IEEE Access
Multidisciplinary ⋮ Rapid Review ⋮ Open Access Journal

Received 18 February 2024, accepted 26 February 2024, date of publication 1 March 2024, date of current version 11 March 2024.

Digital Object Identifier 10.1109/ACCESS.2024.3372136

METHODS

Homoclinic Points Calculation Method With Particle Swarm Optimization

TATSUMI MAKINO[1], YUU MIINO[2], (Member, IEEE), HARUNA MATSUSHITA[3], (Member, IEEE), AND TAKUJI KOUSAKA[1], (Member, IEEE)

[1]Department of Electrical and Electronic Engineering, Chukyo University, Nagoya, Aichi 466-8666, Japan
[2]Graduate School of Education, Naruto University of Education, Naruto, Tokushima 772-8502, Japan
[3]Department of Creative Engineering, Kagawa University, Takamatsu, Kagawa 761-0396, Japan

Corresponding author: Takuji Kousaka (takuji@bifurcation.jp)

This work was supported by Japan Society for the Promotion of Science KAKENHI under Grant JP22K12181 and Grant JP22K12201.

ABSTRACT This paper proposes a novel algorithm to accurately calculate the coordinates of homoclinic points observed in discrete-time dynamical systems. The proposed method is based on the particle swarm optimization method. Compared with the current methods, the proposed methodology has the advantages of not requiring the careful selection of the initial conditions and not requiring information related to the derivative of the objective function. It is shown that the proposed method can successfully obtain the homoclinic points of a system, even if the system parameters are close to those that describe the homoclinic bifurcation sets of the system; this is achieved via the construction of an efficient objective function that depends on the Euclidean distance between the points in each manifold. We apply the developed method to two- and three-dimensional discrete-time dynamical systems and demonstrate the validity of the algorithm via the numerical work. The reliability of the proposed algorithm was achieved by evaluating a metric based on the success rate of the method.

INDEX TERMS Particle swarm optimization, homoclinic points, homoclinic tangency, discrete dynamical systems, global bifurcation.

I. INTRODUCTION

Open questions remain regarding many mechanisms in the natural world across numerous research fields. Mathematical models, including nonlinear systems, are widely used to simulate and analyze such mechanisms. These mathematical models are applied within a huge variety of fields, but they are often similar in their construction as they are frequently based on ordinary differential equations (ODEs) or maps. For example, the Lorenz system is a model used to investigate atmospheric convection; this model is described by a nonlinear system of three ODEs [1]. Izhikevich introduced a model that accurately describes the functioning of neurons; this model includes a system of ODEs and a discrete map that represents neural firing [2]. Chua developed a simple electronic circuit that exhibits chaotic behavior; this model is composed of three ODEs that contain a non-smooth function [3]. Such nonlinear systems frequently exhibit exciting phenomena, including multistability, limit cycles, self-oscillations, bifurcations, and chaos. Chaos has been an active topic of research since its discovery in the late 20th century. Recent work has focused on its underlying mechanisms [4], [5] and has led to the development of technologies that utilize its essential characteristics, such as initial value sensitivity or the existence of dense periodic points; examples of technologies that utilize chaos include image encryption via chaos cryptography [6], modeling new dynamical systems including chaotic systems [7], [8], and synchronization via chaotic neural networks in networked control systems [9].

Smale derived a sufficient criterion to demonstrate the existence of chaos in a system [10]. Smale demonstrated that a diffeomorphism topologically conjugates to the horseshoe map if the discrete dynamical system defined by the

The associate editor coordinating the review of this manuscript and approving it for publication was Hamed Azami.

diffeomorphism has a saddle point and its stable and unstable manifolds contain transversal intersections, which are referred to as homoclinic points. Since the horseshoe map leads to chaotic dynamics, the existence of the transversal homoclinic points indicates the existence of chaotic behavior in the system. In other words, we can confirm the existence of chaos in a nonlinear system by demonstrating that the system contains homoclinic points. Homoclinic points emerge (and disappear) at the specific parameter value at which the stable and unstable manifolds are tangent to each other; this geometric relationship referred to as homoclinic tangency. This phenomenon is considered to be within a class of global bifurcations in discrete-time dynamical systems referred to as homoclinic bifurcations.

To find the homoclinic points or the homoclinic bifurcation parameters of a given system, it is normally necessary to derive the mathematical conditions, called objective functions, for the existence of the homoclinic points and obtain their roots via numerical methods. Numerous methods to approach this problem have been developed, including those proposed in [11], [12], [13], and [14]. The conventional methods used to find the roots of the objective functions require the derivative of the objective functions; Newton's method is widely used in such problems. Key features of algorithms based on Newton's method include:

1) The manual selection of suitable initial values.
2) The calculation of the derivatives of the objective function.
3) Rapid convergence due to its single-point search approach.

Such methods work well and exhibit a good rate of convergence when given suitable initial conditions. However, these methods also have disadvantages, for example, it can be difficult to accurately calculate the derivatives of the objective functions, and the success of such methods is highly dependent on the selection of the initial conditions. In a chaotic situation, the selection of the initial conditions is a difficult problem because the value of the objective function is sensitive to the initial conditions. Even in three-dimensional (3D) systems, previous work [15] has approached the homoclinic point problem by assuming a two-dimensional (2D) plane as a stable manifold despite it is actually a 3D surface.

Techniques other than Newton's method can also be used to find the roots of the objective function in problems related to homoclinic points. In the works [16], [17], a method based on the particle swarm optimization (PSO) [18] was proposed; this method was referred to as the nested-layer particle swarm optimization (NLPSO) algorithm; this algorithm can be used to derive the local bifurcation set. The PSO technique does not require the careful selection of initial values or the derivative of the objective function; the algorithm does not require the stability of the periodic solutions to derive the local bifurcation parameters, including the period-doubling, saddle-node, and Neimark-Sacker bifurcations [19]. In the case of bifurcations that are not classified as local bifurcations, a similar approach to that used in the NLPSO algorithm can be implemented; such an NLPSO-based algorithm can be used to investigate the properties of border-collision bifurcations [20]. However, to date, no study has been conducted to identify a suitable algorithm for use on systems that exhibit homoclinic bifurcations.

A method to obtain the homoclinic points of 2D discrete dynamical systems has initially been considered in our previous works [21], [22]. The proposed method was also based on the PSO algorithm and utilized two PSO algorithms, which were evaluated alternately on the stable and unstable manifolds. However, the previously proposed method cannot obtain the homoclinic points when the parameters describing the system are closer to those of the homoclinic bifurcation sets, i.e., the method cannot be used when the stable and unstable manifolds are asymptotically tangent at the homoclinic points. Advantages of the method proposed here include:

1) Eliminating the manual selection of the initial values via the use of a random candidate initialization.
2) No information related to the derivatives of the objective function is required; this renders our novel method suitable for applications related to complex system.
3) The use of a multi-candidate solution strategy, enhancing the robustness and range of the search space.

In this paper, we propose an innovative algorithm, based on the underlying concepts of the PSO algorithm, which can be used to calculate the exact coordinates of the homoclinic points; the method proposed here overcomes the aforementioned inadequacy of the previously developed algorithm. This work represents an important step in the development of an efficient method for obtaining the homoclinic bifurcation parameters as the proposed method can be used for parameter values that are close to the bifurcation sets. Furthermore, the method can be used to investigate higher-dimensional systems as the objective function is defined in relation to the Euclidean distance between the points in the manifolds.

The rest of this article is organized as follows: Section II demonstrates the advantages of the PSO and outlines the basis of the algorithm. Section III defines a discrete dynamical system, demonstrates that the system contains both stable and unstable manifolds, and derives the conditions for the existence of homoclinic points. Section IV proposes a method to obtain the homoclinic points using a PSO algorithm. We define a new search space and a new objective function that satisfy the previously obtained conditional expressions. Section V presents the results of numerical experiments obtained using the proposed method to investigate the behavior of the 2D and 3D discrete-time dynamical systems and verifies the accuracy of the method. Finally, Section VI presents the conclusions obtained from this work, highlights the importance of this method, and proposes potential directions for further related works.

II. PARTICLE SWARM OPTIMIZATION

The PSO algorithm is a metaheuristic optimization method that models swarm intelligence, such as that exhibited by flocks of birds and schools of fish. PSO generates multiple particles that have both a defined velocity and position within the search space; the particles represent the candidate solutions of the optimization problem. The particles are permitted to move around the search space in search of the optimal solution; the particles are permitted to share information with each other. The PSO algorithm does not require carefully selected initial values or the derivatives of the objective function; both of these features are necessary when using Newton's method. The PSO method accepts changes to the candidate solution in directions that lead to worse solutions as it does not have information related to which directions represent worse directions. The characteristics of the PSO algorithm mean that it can work well in the case of chaotic dynamical systems. The algorithm used in PSO is described below. L particles move in the D-dimensional search space, $\mathbb{R}^D$; these particles search for the minimum value of the objective function $F : \mathbb{R}^D \to \mathbb{R}$. The optimization problem to solve here is defined as follows:

$$\underset{z}{\text{minimize}}\, F(\boldsymbol{z}), \tag{1}$$

where $\boldsymbol{z} = \langle z_1, z_2, \cdots, z_D \rangle \in \mathbb{R}^D$ is a D-variable vector, which represents the position of a particle. In the implementation of the PSO algorithm, we use the termination criterion, C, and we impose a maximum number of iterations, T, i.e., the calculation terminates when the inequality $F(\boldsymbol{z}) \leq C$ is satisfied or the number of iterations undertaken is equal to T. The velocity and position of each particle are defined by

$$\boldsymbol{u}^i(t) = \left\langle u_1^i(t), u_2^i(t), \cdots, u_j^i(t), \cdots, u_D^i(t) \right\rangle, \tag{2}$$

$$\boldsymbol{z}^i(t) = \left\langle z_1^i(t), z_2^i(t), \cdots, z_j^i(t), \cdots, z_D^i(t) \right\rangle, \tag{3}$$

respectively, where $t \in \mathbb{N}$ represents the discrete time, which corresponds to the number of time iterations, $i = 1, \ldots, L$ is the identifier for each particle, and $j = 1, \ldots, D$ is the identifier for each dimension. Each particle is given an initial velocity of $\boldsymbol{0}$, i.e., $\boldsymbol{u}^i(t) = \boldsymbol{0}$ for all i, and a random initial position in $\mathbb{R}^D$. The velocity and position are updated via the following rules

$$\begin{aligned} u_j^i(t+1) &= w u_j^i(t) + c_1 r_1 \left[p_j^i(t) - z_j^i(t) \right] \\ &\quad + c_2 r_2 \left[g_j(t) - z_j^i(t) \right], \\ z_j^i(t+1) &= z_j^i(t) + u_j^i(t+1), \end{aligned} \tag{4}$$

where $\boldsymbol{p}^i(t) = \left\langle p_1^i(t), \ldots, p_j^i(t), \ldots, p_D^i(t) \right\rangle \in \mathbb{R}^D$ represents the vector satisfying the minimum value of the objective function in the search history of the i-th particle at time t, which is referred to as pbest, and $\boldsymbol{g}(t) = \left\langle g_1(t), \ldots, g_j(t), g_D(t) \right\rangle \in \mathbb{R}^D$ is the vector satisfying the minimum value of the objective function in the search history of all particles at time t, which is referred to as gbest, w is the inertial weight, c_1 and c_2 are the acceleration coefficients, and r_1 and r_2 are appropriate random numbers within the range 0 to 1. The values of pbest and gbest are updated immediately after calculating (4). The PSO continues updating until the termination criteria is met. When the PSO algorithm terminates, the search result is given by the final value of gbest.

III. HOMOCLINIC POINTS

We consider an n-dimensional discrete-time dynamical system defined by

$$\boldsymbol{x}(k+1) = \boldsymbol{f}_\lambda\left(\boldsymbol{x}(k)\right), \tag{5}$$

where $\boldsymbol{f}_\lambda : \mathbb{R}^n \to \mathbb{R}^n$ represents a diffeomorphism, $k \in \mathbb{Z}$ indicates the discrete time, $\boldsymbol{x}(k) \in \mathbb{R}^n$ is the state variable at discrete time k, and $\lambda \in \mathbb{R}^r$ is a vector that represents the system parameter. Here, we denote the l-th functional power as $\boldsymbol{f}_\lambda^l = \boldsymbol{f}_\lambda \circ \boldsymbol{f}_\lambda \circ \cdots \circ \boldsymbol{f}_\lambda$. A point $\boldsymbol{x}_p$ is said to be an l-periodic point if $\boldsymbol{x}_p$ satisfies the following criteria:

$$\boldsymbol{x}_p = \boldsymbol{f}_\lambda^l(\boldsymbol{x}_p) \quad \text{and} \quad \boldsymbol{x}_p \neq \boldsymbol{f}_\lambda^q(\boldsymbol{x}_p) \quad \text{for} \quad q \in (0, l) \subset \mathbb{Z}. \tag{6}$$

The Jacobian matrix of $\boldsymbol{f}_\lambda^l$, denoted $\mathbf{J}_{\boldsymbol{f}_\lambda^l}$, at an l-periodic point $\boldsymbol{x}_p$ is given by

$$\mathbf{J}_{\boldsymbol{f}_\lambda^l}(\boldsymbol{x}_p) = \left.\frac{\partial \boldsymbol{f}_\lambda^l}{\partial \boldsymbol{x}}\right|_{\boldsymbol{x}=\boldsymbol{x}_p} = \prod_{q=1}^{l} \left.\frac{\partial \boldsymbol{f}_\lambda}{\partial \boldsymbol{x}}\right|_{\boldsymbol{x}=\boldsymbol{f}_\lambda^{l-q}(\boldsymbol{x}_p)}. \tag{7}$$

The asymptotic stability of an l-periodic point $\boldsymbol{x}_p$ can be evaluated by considering the eigenvalues of $\mathbf{J}_{\boldsymbol{f}_\lambda^l}(\boldsymbol{x}_p)$, which are the scalar values that satisfy the following equation:

$$\mathbf{J}_{\boldsymbol{f}_\lambda^l}(\boldsymbol{x}_p)\boldsymbol{v} = \mu \boldsymbol{v}, \tag{8}$$

where $\mu \in \{\mu_1, \mu_2, \ldots, \mu_n\}$ represents an eigenvalue of $\mathbf{J}_{\boldsymbol{f}_\lambda^l}(\boldsymbol{x}_p)$, and $\boldsymbol{v} \in \left\{\boldsymbol{v}_{\mu_1}, \boldsymbol{v}_{\mu_2}, \ldots, \boldsymbol{v}_{\mu_n}\right\}$ is the corresponding eigenvector. In this study, we consider eigenvectors with a unit norm, i.e., $\|\boldsymbol{v}\| = 1$. It is known that the periodic point $\boldsymbol{x}_p$ is asymptotically stable if $0 < |\mu| < 1$ and unstable if $|\mu| > 1$; such periodic points are referred to as hyperbolic periodic points. A hyperbolic periodic point can be roughly classified into one of the following three types: a completely stable point (if $\forall \mu, |\mu| < 1$), a completely unstable point (if $\forall \mu, |\mu| > 1$), and a saddle point (otherwise). Considering a saddle point $\boldsymbol{x}_p$, we can classify the eigenvectors of $\mathbf{J}_{\boldsymbol{f}_\lambda}(\boldsymbol{x}_p)$ into two sets:

$$V^s = \left\{ \boldsymbol{v} \;\middle|\; \left[\mathbf{J}_{\boldsymbol{f}_\lambda^l}(\boldsymbol{x}_p) - \mu\right]\boldsymbol{v} = \boldsymbol{0},\ 0 < |\mu| < 1 \right\}, \tag{9}$$

$$V^u = \left\{ \boldsymbol{v} \;\middle|\; \left[\mathbf{J}_{\boldsymbol{f}_\lambda^l}(\boldsymbol{x}_p) - \mu\right]\boldsymbol{v} = \boldsymbol{0},\ 1 < |\mu| \right\}. \tag{10}$$

Then, the linear subspaces of $\mathbb{R}^n$ spanned by V^s and V^u are referred to as the stable and unstable subspace,

$$E^s = \text{span}\left(V^s\right), \tag{11}$$

$$E^u = \text{span}\left(V^u\right), \tag{12}$$

respectively.

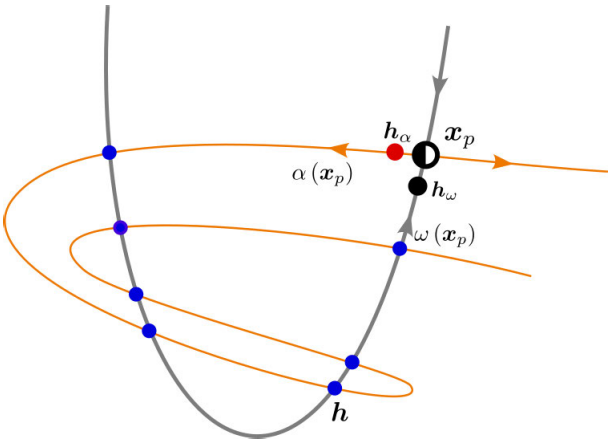

FIGURE 1. Example of an unstable manifold $\alpha(x_p)$ (orange curve), a stable manifold $\omega(x_p)$ (gray curve), and all homoclinic points h (blue dots). The half-filled black point represents an l-periodic saddle point x_p.

In the system defined by (5), assuming $\boldsymbol{x}_p$ is a hyperbolic l-periodic point, some trajectories of the system enter or exit the point $\boldsymbol{x}_p$; all points on these trajectories construct a $\boldsymbol{f}_\lambda^l$-invariant manifold, referred to as a stable or unstable manifolds. If $\boldsymbol{x}_p$ is a saddle point, the unstable and stable manifolds are respectively defined by the following expressions:

$$\alpha(\boldsymbol{x}_p) = \left\{ \boldsymbol{x} \in \mathbb{R}^n \;\middle|\; \lim_{m\to\infty} \boldsymbol{f}_\lambda^{-lm}(\boldsymbol{x}) = \boldsymbol{x}_p \right\}, \tag{13}$$

$$\omega(\boldsymbol{x}_p) = \left\{ \boldsymbol{x} \in \mathbb{R}^n \;\middle|\; \lim_{m\to\infty} \boldsymbol{f}_\lambda^{lm}(\boldsymbol{x}) = \boldsymbol{x}_p \right\}, \tag{14}$$

where $\boldsymbol{f}_\lambda^{-lm} = \left(\boldsymbol{f}_\lambda^{-l}\right)^m$ is the m-th functional power of $\boldsymbol{f}_\lambda^{-l}$, which represents the inverse of $\boldsymbol{f}_\lambda^l$. As is proven by the Hartman–Grobman theorem, E^u and E^s are the tangent spaces of $\alpha(\boldsymbol{x}_p)$ and $\omega(\boldsymbol{x}_p)$ at $\boldsymbol{x}_p$, respectively. In other words, the geometric structures of each manifold with respect to $\boldsymbol{x}_p$ are determined by the values of the stable and unstable eigenvalues. Let $\mathcal{H}$ be a subset of $\mathbb{R}^n$ given by

$$\mathcal{H} = \left(\alpha(\boldsymbol{x}_p) \cap \omega(\boldsymbol{x}_p)\right) \setminus \boldsymbol{x}_p, \tag{15}$$

then all the points in $\mathcal{H}$ are referred to as homoclinic points. We note here that $\mathcal{H}$ is $\boldsymbol{f}_\lambda^l$-invariant by definition; that is, if there is one homoclinic point $\boldsymbol{h} \in \mathcal{H}$, the set $\mathcal{H}$ includes infinitely many homoclinic points, including its image and preimage of $\boldsymbol{h}$ under $\boldsymbol{f}_\lambda^{lm}$ for any value of m. Geometrically, the homoclinic points represent the points where the stable and unstable manifolds intersect. Homoclinic points are referred to as being transversal at those points where the manifolds are transversal. Fig. 1 shows an example of a 2D discrete dynamical system, which exhibits a stable and an unstable manifold of a saddle point, $\boldsymbol{x}_p$, transversally intersecting at all homoclinic points. Each manifold is a one-dimensional curve in this case.

In this example, the manifolds are one-dimensional (1D) curves. Assuming the existence of a homoclinic point, $\boldsymbol{h}$, we can describe the homoclinic points that are present in the unstable and stable subspaces, denoted by $\boldsymbol{h}_\alpha$ and $\boldsymbol{h}_\omega$, as

$$\boldsymbol{h}_\alpha = \boldsymbol{f}_\lambda^{-lM}(\boldsymbol{h}), \tag{16}$$

$$\boldsymbol{h}_\omega = \boldsymbol{f}_\lambda^{lN}(\boldsymbol{h}), \tag{17}$$

where M and N are integers that are sufficiently large for $\boldsymbol{h}_\alpha$ and $\boldsymbol{h}_\omega$, respectively, to be located within the neighborhood of $\boldsymbol{x}_p$. Eliminating $\boldsymbol{h}$ from (16) and (17),, we obtain the expression

$$\boldsymbol{f}_\lambda^{lM}(\boldsymbol{h}_\alpha) = \boldsymbol{f}_\lambda^{-lN}(\boldsymbol{h}_\omega). \tag{18}$$

Equation (18) can be computed as we can evaluate (18) by considering the map $\boldsymbol{f}_\lambda$ and the points in the sets $\alpha(\boldsymbol{x}_p)$ and $\omega(\boldsymbol{x}_p)$ around $\boldsymbol{x}_p$, $\boldsymbol{h}_\alpha$, and $\boldsymbol{h}_\omega$; $\boldsymbol{h}_\alpha$ and $\boldsymbol{h}_\omega$ are obtained by considering $\boldsymbol{x}_p$ and the vectors in E^u and E^s. For example, in a 2D system, considering the 1D manifolds, we can manipulate $\boldsymbol{h}_\alpha$ and $\boldsymbol{h}_\omega$ in two distinct ways: we can scale the eigenvectors, and we can utilize the iteration counts of mappings, M and N. M and N can be selected freely subject to the restriction that they are large integers.

Table 1 summarizes the variables used to parameterize the discrete dynamical systems considered in this work.

TABLE 1. Variables and their symbols of discrete dynamical systems.

Variable	Symbol
Evolution function	$\boldsymbol{f}_\lambda$
State variable vector	$\boldsymbol{x}$
Discrete time	k
System parameter vector	$\boldsymbol{\lambda}$
Dimension of the state space	n
Number of system parameters	r
Number of periods of the periodic point	l
An l-periodic point	$\boldsymbol{x}_p$
Iterator of $\boldsymbol{f}_\lambda$	q
Eigenvalue of $\mathbf{J}_{\boldsymbol{f}_\lambda}$	μ
Eigenvector of $\mathbf{J}_{\boldsymbol{f}_\lambda}$	$\boldsymbol{v}$
Set of $\boldsymbol{v}$ for $\boldsymbol{x}_p$ with $\lvert\mu\rvert > 1$	V^u
Set of $\boldsymbol{v}$ for $\boldsymbol{x}_p$ with $0 < \lvert\mu\rvert < 1$	V^s
Unstable subspace spanned by V^u	E^u
Stable subspace spanned by V^s	E^s
Unstable manifold of $\boldsymbol{x}_p$	$\alpha(\boldsymbol{x}_p)$
Stable manifold of $\boldsymbol{x}_p$	$\omega(\boldsymbol{x}_p)$
Iterator of $\boldsymbol{f}_\lambda^l$	m
Set of homoclinic points	$\mathcal{H}$
Homoclinic point	$\boldsymbol{h}$
Homoclinic point in E^u	$\boldsymbol{h}_\alpha$
Homoclinic point in E^s	$\boldsymbol{h}_\omega$

IV. METHOD FOR CALCULATING HOMOCLINIC POINTS VIA PSO

The homoclinic points for an l-periodic point $\boldsymbol{x}_p$ are obtained by solving (18) for $\boldsymbol{h}_\alpha$ and $\boldsymbol{h}_\omega$; both these solutions and the images/preimages are homoclinic points, including $\boldsymbol{h}$ in (16) and (17). In the conventional method [12], (18) is solved using Newton's method. In this section, we develop a calculation method based on the PSO to obtain the homoclinic points; we call this method the PSO_{hp} method. The algorithm presented here is based on the application of the PSO; the variables, search space, and the objective function are set such that the PSO algorithm yields the conditions of homoclinic points.

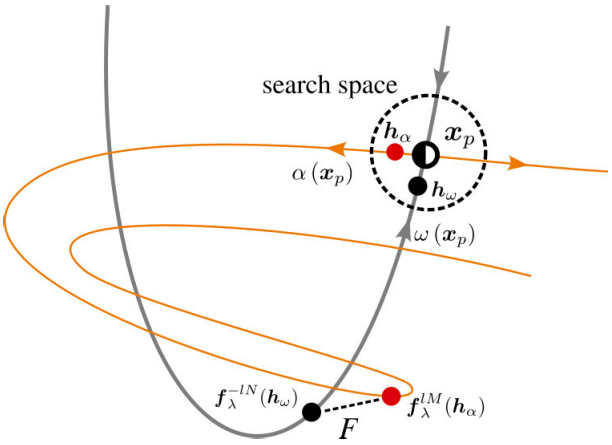

FIGURE 2. Geometric interpretation of the search space and objective function considered in the $\mathrm{PSO_{hp}}$ method.

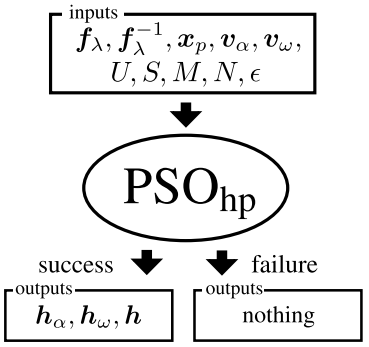

FIGURE 3. Inputs and outputs of the $\mathrm{PSO_{hp}}$ algorithm.

First, we describe the search space and the objective function used in the $\mathrm{PSO_{hp}}$ method. Fig. 2 outlines the geometric concept that underlies the search space and the objective function of the $\mathrm{PSO_{hp}}$ method, as it would be applied to the example problem depicted in Fig. 1. We define that the search spaces, i.e., the tangent spaces of the manifolds at $\boldsymbol{x}_p$ within the dotted circle shown in Fig. 2, are the stable and unstable manifolds around $\boldsymbol{x}_p$. Let $U = \dim E^u$, $S = \dim E^s$, $Z^u \subset \mathbb{R}^U$, and $Z^s \subset \mathbb{R}^S$, and we define the coefficient vectors $\boldsymbol{z}_\alpha = \langle z_{\alpha 1}, z_{\alpha 2}, \ldots, z_{\alpha U}\rangle \in Z^u$ and $\boldsymbol{z}_\omega = \langle z_{\omega 1}, z_{\omega 2}, \ldots, z_{\omega S}\rangle \in Z^s$; the points in $\alpha(\boldsymbol{x}_p)$ or $\omega(\boldsymbol{x}_p)$ around $\boldsymbol{x}_p$ are then represented by a function including a linear combination of $\boldsymbol{v}_{\alpha m} \in V^u$ or $\boldsymbol{v}_{\omega m} \in V^s$, i.e.,

$$H_\alpha : Z^u \to \mathbb{R}^n; \boldsymbol{z}_\alpha \mapsto \boldsymbol{x}_p + \sum_{m=1}^{U} z_{\alpha m}\boldsymbol{v}_{\alpha m}, \tag{19}$$

$$H_\omega : Z^s \to \mathbb{R}^n; \boldsymbol{z}_\omega \mapsto \boldsymbol{x}_p + \sum_{m=1}^{S} z_{\omega m}\boldsymbol{v}_{\omega m}. \tag{20}$$

Equations (19) and (20) are not satisfied if the point $H_\alpha(\boldsymbol{z}_\alpha)$ or $H_\omega(\boldsymbol{z}_\omega)$ is too far from $\boldsymbol{x}_p$ because such a point is not in $\alpha(\boldsymbol{x}_p)$ or $\omega(\boldsymbol{x}_p)$. In other words, given a positive $\epsilon \ll 1$, the search spaces Z^u and Z^s can be defined as being within the ranges $0 < \|\boldsymbol{z}_\alpha\| < \epsilon$ and $0 < \|\boldsymbol{z}_\omega\| < \epsilon$, respectively. Then, there exist $\gamma_\alpha \in Z^u$ and $\gamma_\omega \in Z^s$ that satisfy

$$\boldsymbol{h}_\alpha = H_\alpha(\gamma_\alpha), \tag{21}$$

$$\boldsymbol{h}_\omega = H_\omega(\gamma_\omega), \tag{22}$$

if $\mathcal{H} \neq \emptyset$. We can thus implement the $\mathrm{PSO_{hp}}$ method to search for γ_α and γ_ω. Substituting $\boldsymbol{h}_\alpha$ and $\boldsymbol{h}_\omega$ from (21) and(22) into (18), we obtain

$$\boldsymbol{f}_\lambda^{lM} \circ H_\alpha(\gamma_\alpha) - \boldsymbol{f}_\lambda^{-lN} \circ H_\omega(\gamma_\omega) = \boldsymbol{0}. \tag{23}$$

Thus, we can define the objective function for the $\mathrm{PSO_{hp}}$ method as

$$F(\boldsymbol{z}_{\mathrm{hp}}) = \|\boldsymbol{f}_\lambda^{lM} \circ H_\alpha(\boldsymbol{z}_\alpha) - \boldsymbol{f}_\lambda^{-lN} \circ H_\omega(\boldsymbol{z}_\omega)\|, \tag{24}$$

where $\boldsymbol{z}_{\mathrm{hp}} = \boldsymbol{z}_\alpha \,\|\, \boldsymbol{z}_\omega = \langle z_{\alpha 1}, z_{\alpha 2}, \ldots, z_{\alpha U}, z_{\omega 1}, z_{\omega 2}, \ldots, z_{\omega S}\rangle \in Z^{\mathrm{hp}} = Z^u \oplus Z^s \subset \mathbb{R}^n$ is a vector corresponding to the position of a particle, which is composed of the coefficient vectors $\boldsymbol{z}_\alpha$ and $\boldsymbol{z}_\omega$. Following the same convention as that used in (3), we denote the position of the i-th particle at time t using $\boldsymbol{z}_{\mathrm{hp}}^i(t)$. The objective function defined in (24) yields the Euclidean norm between two points (the point in $\alpha(\boldsymbol{x}_p)$ and the point in $\omega(\boldsymbol{x}_p)$). We note that the objective function F does not evaluate the Euclidean norm between $\boldsymbol{h}_\alpha$ and $\boldsymbol{h}_\omega$. Obtaining the parameters for which the objective function is equal to zero is synonymous with the precise determination of the homoclinic point conditions, thus the termination criterion, C, of the PSO algorithm is a direct measure of the accuracy of the parameters describing the obtained homoclinic points (smaller values of C signify higher precision) In addition, as mentioned in Section III, the integers M and N should be large. If the value of M or N is not great enough, either or both the homoclinic point $\boldsymbol{h}_\alpha$ or $\boldsymbol{h}_\omega$ satisfying (24) will not be within the neighborhood of $\boldsymbol{x}_p$.

Here, we describe the procedure used to obtain the homoclinic point using the $\mathrm{PSO_{hp}}$ method. By selecting appropriate values for the system parameters, it is possible to obtain the l-periodic point $\boldsymbol{x}_p$ whose stable and unstable manifolds exhibit transversal intersections. We can obtain $\boldsymbol{x}_p$ by analytically solving a set of equations or via a numerical method, such as that developed in [23]. It is then possible to calculate the eigenvalues and eigenvectors of $\mathbf{J}_{\boldsymbol{f}^l}(\boldsymbol{x}_p)$ and separate the eigenvectors into the two subsets V^u and V^s by evaluating their corresponding eigenvalues; these values are used to define the functions H_α and H_ω. Using the objective function, F, depending on $\boldsymbol{f}_\lambda$, H_α, and H_ω for $\boldsymbol{x}_p$, and sufficiently large values of M and N, the $\mathrm{PSO_{hp}}$ method can be used to calculate the optimal solution.

Algorithm 1 shows the pseudocode of the $\mathrm{PSO_{hp}}$ method. We randomly initialize the position vectors $\boldsymbol{z}_{\mathrm{hp}}^i(0)$ in the search space Z^{hp} and set the initial velocity vectors $\boldsymbol{u}_{hp}^i(0) = \boldsymbol{u}_\alpha^i(0) \,\|\, \boldsymbol{u}_\omega^i(0)$ to be $\boldsymbol{0}$ to prevent the particles from leaving the search space while t is small. The objective function F is then evaluated for each iteration count t and each particle i; the values of pbest, $\boldsymbol{p}_{\mathrm{hp}}^i = \boldsymbol{p}_\alpha^i \,\|\, \boldsymbol{p}_\omega^i$, and gbest, $\boldsymbol{g}_{\mathrm{hp}} = \boldsymbol{g}_\alpha \,\|\, \boldsymbol{g}_\omega$, are updated immediately after the evaluation. The

Algorithm 1 Pseudocode of the PSO_{hp} Method. In the Implementation, the Inputs Z^u and Z^s Can Be Replaced by ϵ

Input: F, Z^u, Z^s, L, T, C
Output: $\boldsymbol{g}_{\text{hp}}$ leading the optimal homoclinic points around $\boldsymbol{x}_p$

$t \leftarrow 0$; ▷ Initialize the iterator
forall $i \in [1, L]$ **do** ▷ Iterate through the swarm
  $\boldsymbol{u}^i_{hp}(0) \leftarrow$ a zero vector; ▷ Initialize velocity
  $\boldsymbol{z}^i_{\text{hp}}(0) \leftarrow$ a random vector in Z^{hp}; ▷ Initialize position
  $\boldsymbol{p}^i_{\text{hp}}(0) \leftarrow \boldsymbol{z}^i_{\text{hp}}(0)$; ▷ Initialize pbest
$\boldsymbol{g}_{\text{hp}}(0) \leftarrow$ the best of all pbest; ▷ Initialize gbest
repeat
  forall $i \in [1, L]$ **do** ▷ Iterate through the swarm
    Apply (4); ▷ Update velocity and position
    if $F\left(\boldsymbol{z}^i_{hp}(t+1)\right) < F\left(\boldsymbol{p}^i_{hp}(t)\right)$ **then** ▷ If a better z_{hp} is found
      $\boldsymbol{p}^i_{\text{hp}}(t+1) \leftarrow \boldsymbol{z}^i_{\text{hp}}(t+1)$; ▷ Update pbest
      if $F\left(\boldsymbol{p}^i_{hp}(t+1)\right) < F\left(\boldsymbol{g}_{hp}(t)\right)$ **then** ▷ If a better $\boldsymbol{p}^i_{\text{hp}}$ is found
        $\boldsymbol{g}_{\text{hp}}(t+1) \leftarrow \boldsymbol{z}^i_{\text{hp}}(t+1)$; ▷ Update gbest
  $t \leftarrow t+1$;
until $t \geq T$ *or* $F(\boldsymbol{g}_{hp}(t)) < C$;
return $\boldsymbol{g}_{hp}(t)$

velocity and position vectors of each particle are then updated using the recurrence relation defined in (4). We note that a particle can take a position that is out of the search space during the update even though such positions are not taken as potential values for pbest or gbest. The loop that updates the velocity and position vectors via (4) continues while $F(\boldsymbol{g}_{\text{hp}}) \geq C$ and $t < T$, where T is the preset maximum number of iterations. If $F(\boldsymbol{g}_{\text{hp}}) < C$ is satisfied, the optimal solution $\boldsymbol{g}_{\text{hp}}$ has been obtained; this value can then be used to calculate the homoclinic points by $H_\alpha(\boldsymbol{g}_\alpha)$ and $H_\omega(\boldsymbol{g}_\omega)$. The homoclinic point $\boldsymbol{h}$ can then be calculated by considering $\boldsymbol{f}_\lambda^{lM} \circ H_\alpha(\boldsymbol{g}_\alpha)$ or $\boldsymbol{f}_\lambda^{-lN} \circ H_\omega(\boldsymbol{g}_\omega)$. The precision with which the coordinates of homoclinic points are computed is closely linked to the termination criterion C; this parameter can be used to control the accuracy of the calculation process. Fig. 3 presents a schematic showing the variables that are given as inputs into the PSO_{hp} algorithm for the computation of the homoclinic points. In this figure, "success" is defined when the conditions $F(\boldsymbol{g}_{\text{hp}}) < C$ and $t < T$ are met, and any other outcome is given by "failure". The PSO_{hp} method can also be used to obtain the l-periodic point $\boldsymbol{x}_p$ (rather than the homoclinic points) as the method searches for the intersection of the unstable and stable manifolds. On the other hand, the swarm does not converge or converges to $\boldsymbol{x}_p$ if the system is such that $\mathcal{H} = \emptyset$. In contrast with traditional methods that utilize the entire state space, our approach focuses on the stable and unstable manifolds in the vicinity of a saddle point; this significantly reduces the sensitivity of this method to the initial conditions compared with the traditional methods. Furthermore, due to the derivative-free nature of the optimization method used here (the PSO), our method is applicable in situations where the calculation of derivatives is either arduous or impossible.

Table 2 summarizes the variables used in the PSO_{hp} algorithm. In addition, we note that it is necessary to manually configure the parameters in (4) to ensure that the method successfully finds the objective solution.

TABLE 2. Variables and their symbols used in the PSO_{hp} method.

Variables	Symbols
Particle index	i
Iterator of searching loop	t
Velocity vector	$\boldsymbol{u}^i_{\text{hp}} = \boldsymbol{u}^i_\alpha \parallel \boldsymbol{u}^i_\omega$
Position vector	$\boldsymbol{z}^i_{\text{hp}} = \boldsymbol{z}^i_\alpha \parallel \boldsymbol{z}^i_\omega$
pbest vector	$\boldsymbol{p}^i_{\text{hp}} = \boldsymbol{p}^i_\alpha \parallel \boldsymbol{p}^i_\omega$
gbest vector	$\boldsymbol{g}_{\text{hp}} = \boldsymbol{g}_\alpha \parallel \boldsymbol{g}_\omega$
Objective function	F
Search space	$Z^{\text{hp}} = Z^u \oplus Z^s$
Controlling parameter for search space	ϵ
Number of particles	L
Termination criterion for t	T
Termination criterion for $F(z_{\text{hp}})$	C

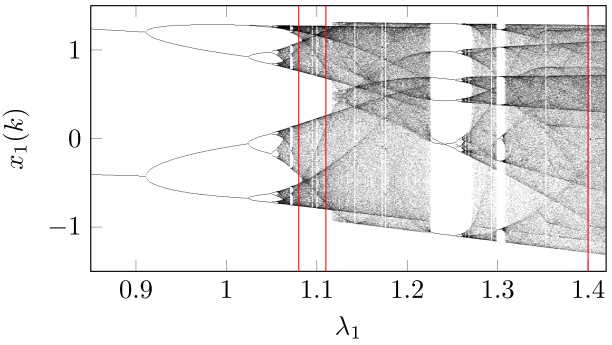

FIGURE 4. One-parameter bifurcation diagram of the Hénon map defined by (25) for $\lambda_1 \in [0.85, 1.42]$ and $\lambda_2 = 0.30$. The red lines from right to left indicate $\lambda_1 = 1.40$, $\lambda_1 = 1.11$, and $\lambda_1 = 1.08$.

V. NUMERICAL EXPERIMENTS

A. HÉNON MAP

In this section, we demonstrate how the proposed method can be applied to a typical 2D discrete-time dynamical system; here, we consider the Hénon map [24], which is defined by a nonlinear map $\boldsymbol{f}_\lambda$:

$$\boldsymbol{f}_\lambda : \mathbb{R}^2 \to \mathbb{R}^2; \boldsymbol{x} \mapsto \boldsymbol{f}_\lambda(\boldsymbol{x}) = \begin{bmatrix} 1 - \lambda_1 x_1^2 + x_2 \\ \lambda_2 x_1 \end{bmatrix}, \quad (25)$$

where $\boldsymbol{x} = \langle x_1, x_2 \rangle \in \mathbb{R}^2$ is the state variables vector and $\lambda = \langle \lambda_1, \lambda_2 \rangle \in \mathbb{R}^2$ is the system parameters vector. The

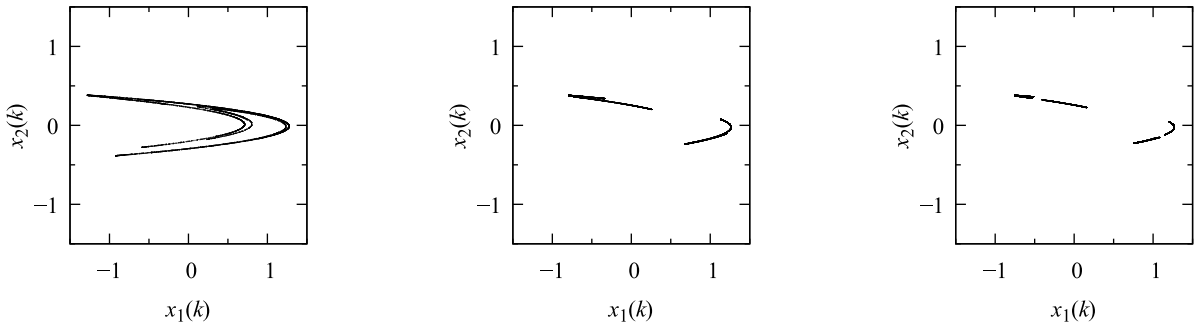

(a) $\lambda_1 = 1.4$. (b) $\lambda_1 = 1.11$. (c) $\lambda_1 = 1.08$.

FIGURE 5. The chaotic attractors of the Hénon map defined by (25).

TABLE 3. The periodic points of the Hénon map with $\lambda_2 = 0.30$; these values are used in the numerical work presented here. I^l is used to denote the l-periodic point considered here.

I^l	$\boldsymbol{x}_p = \langle x_{1p}, x_{2p} \rangle$	l	λ_1	$\boldsymbol{v}_\alpha$	$\boldsymbol{v}_\omega$
I^1	$\langle 0.631355, 0.189406 \rangle$	1	1.40	$\langle 0.988, -0.154 \rangle$	$\langle 0.461, 0.887 \rangle$
I^2	$\langle -0.460977, 0.327482 \rangle$	2	1.11	$\langle 0.990, -0.143 \rangle$	$\langle 0.751, -0.660 \rangle$
I^4	$\langle 0.009794, 0.255081 \rangle$	4	1.08	$\langle 0.983, -0.181 \rangle$	$\langle 0.990, 0.140 \rangle$

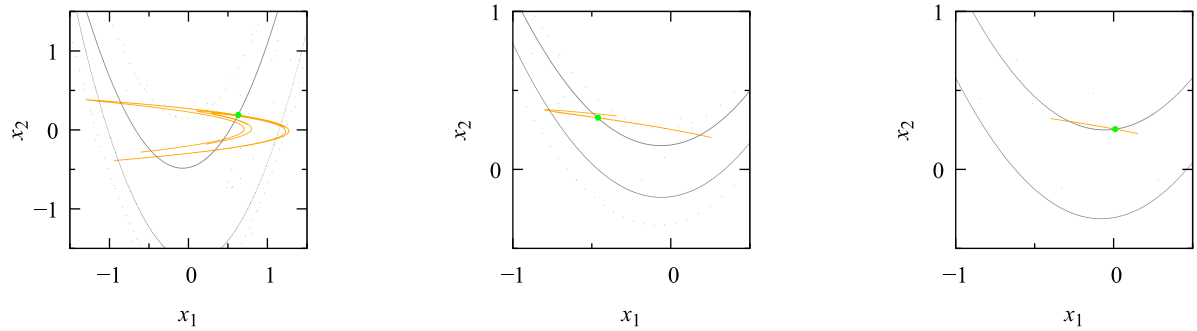

(a) I^1. (b) I^2. (c) I^4.

FIGURE 6. The unstable manifold (orange dots) and stable manifold (gray dots) corresponding to each periodic point (green dots) in the Hénon map.

Hénon map is known to be chaotic for $\lambda = \langle 1.40, 0.30 \rangle$; for this parameter value, there exist homoclinic points in the state space. Fig. 4 shows the one-parameter bifurcation diagram of the system, calculated from left to right. At the parameter values indicated by the red lines in Fig. 4, the chaotic attractor exists in the distinct one, two, or four region(s), which can be seen from the right to the left of the figure. Fig. 5 shows the chaotic attractors corresponding to the parameter values indicated by the red lines in Fig. 4; thus, we can observe the distinct regions of each attractor. At these parameter values, we see that there are homoclinic points associated with 1-, 2-, and 4-periodic saddle points.

Here, we show how the PSO_{hp} method can be used to obtain the homoclinic points with the parameters introduced above. We use the periodic points specified in Table 3. Each periodic point listed in Table 3 is identified as a saddle point, possessing one unstable and one stable eigenvector; thus, given dimensionality of the stable and unstable eigenspaces within 2D Hénon map, we see that $U = S = 1$. Fig. 6 depicts the unstable and stable manifolds for each of the

TABLE 4. Values used in the implementation of the PSO_{hp} method related to the Hénon map.

Parameter	Value
Search space range	$\epsilon = 0.001$
Number of particles	$L = 100$
Termination criterion for t	$T = 3000$
Termination criterion for $F(z_{\text{hp}})$	$C = 1 \times 10^{-5}$
Inertial weight	$w = 0.729$
Acceleration coefficients	$c_1 = c_2 = 1.494$
Random numbers	$r_1, r_2 \in [0, 1]$

TABLE 5. Result of numerical experiments for the Hénon map.

I^l	$\boldsymbol{h}$	γ_α	γ_ω	t
I^1	$\langle 0.3411, -0.2526\rangle$	-2.908×10^{-4}	-6.043×10^{-5}	693
	$\langle 0.5995, 0.1294\rangle$	4.775×10^{-4}	-6.407×10^{-6}	606
	$\langle -0.3936, -0.3360\rangle$	-6.084×10^{-4}	-2.422×10^{-4}	1984
	$\langle -0.8424, 0.3346\rangle$	3.499×10^{-5}	-3.877×10^{-4}	1057
	$\langle 0.6020, 0.1342\rangle$	3.219×10^{-4}	-5.887×10^{-6}	1474
I^2	$\langle 0.1848, 0.2179\rangle$	-4.757×10^{-7}	-9.403×10^{-5}	738
	$\langle -0.4596, 0.3262\rangle$	-7.798×10^{-4}	-2.415×10^{-7}	763
	$\langle -0.4610, 0.3275\rangle$	7.062×10^{-4}	-6.789×10^{-9}	2419
	$\langle -0.4901, 0.3540\rangle$	-2.061×10^{-4}	4.605×10^{-6}	1259
	$\langle 0.1851, 0.2181\rangle$	-5.791×10^{-4}	-9.407×10^{-5}	857
I^4	$\langle -0.2789, 0.3038\rangle$	8.235×10^{-4}	-4.849×10^{-6}	512
	$\langle -0.2787, 0.3037\rangle$	2.938×10^{-4}	-4.849×10^{-6}	2071
	$\langle 0.0098, 0.2551\rangle$	-5.896×10^{-4}	4.388×10^{-10}	2203
	$\langle 0.0120, 0.2553\rangle$	-1.854×10^{-4}	1.969×10^{-8}	2627
	$\langle -0.2788, 0.3038\rangle$	7.238×10^{-4}	-4.850×10^{-6}	1532

TABLE 6. Numerically calculated images of h_α and h_ω under the functional power of f_λ and f_λ^{-1}, respectively, for I^1 of the Hénon map. $f_\lambda^0 = \mathrm{id}$ is the identity function, i.e., $f_\lambda^0(x) = x$. For the forward mapping, f_λ, $m \in [0, M] = [0, 50] \subset \mathbb{Z}$; for the backward mapping, f_λ^{-1}, $m \in [0, N] = [0, 5] \subset \mathbb{Z}$.

m	$f_\lambda^m(\boldsymbol{h}_\alpha)$	m	$f_\lambda^{-m}(\boldsymbol{h}_\omega)$
0	$\langle 0.63106717, 0.18945115\rangle$	0	$\langle 0.63132660, 0.18935272\rangle$
⋮	⋮	⋮	⋮
48	$\langle 1.11142059, -0.11253195\rangle$	3	$\langle 0.62401201, 0.17535589\rangle$
49	$\langle -0.84188996, 0.33342618\rangle$	4	$\langle 0.58451962, 0.10234048\rangle$
50	$\langle 0.34113598, -0.25256699\rangle$	5	$\langle 0.34113492, -0.25255813\rangle$

periodic points given in Table 3. We note that the manifolds are depicted by plotting a set of distinct points (thus some discontinuities can be observed in the curves). In Figs. 6(a) to 6(c), we can observe homoclinic points as the transversal intersections of the unstable and stable manifolds. We note that the search variables z_α and z_ω are scalars $z_\alpha = z_{\alpha 1}$ and $z_\omega = z_{\omega 1}$, and H_α and H_ω are described by

$$H_\alpha(z_\alpha) = \boldsymbol{x}_p + z_{\alpha 1}\boldsymbol{v}_{\alpha 1}, \tag{26}$$

$$H_\omega(z_\omega) = \boldsymbol{x}_p + z_{\omega 1}\boldsymbol{v}_{\omega 1}. \tag{27}$$

Thus, following (24), the objective function, F, can be written as

$$F(z_{\mathrm{hp}}) = \sqrt{\begin{array}{l}\left[f_1^{lM} \circ H_\alpha(z_\alpha) - f_1^{-lN} \circ H_\omega(z_\omega)\right]^2 \\ +\left[f_2^{lM} \circ H_\alpha(z_\alpha) - f_2^{-lN} \circ H_\omega(z_\omega)\right]^2\end{array}}, \tag{28}$$

where $\boldsymbol{f}_\lambda = \langle f_1, f_2\rangle$. Table 4 shows the values of the parameters used in the implementation of the $\mathrm{PSO_{hp}}$ method for this investigation, and is based on [25].

Next, we explain how to select suitable values for the mapping numbers M and N. The mapping numbers must be set to take large values to ensure that both $\boldsymbol{h}_\alpha$ and $\boldsymbol{h}_\omega$ are located within the neighborhood of $\boldsymbol{x}_p$. However, since high sensitivity to the initial values is typical of systems that exhibit chaotic behavior, the selection of a larger value of M and/or N can lead to z_α or z_ω having a large influence on the objective function F. It is necessary to find suitable values for M and N manually. In this study, we set the value of M

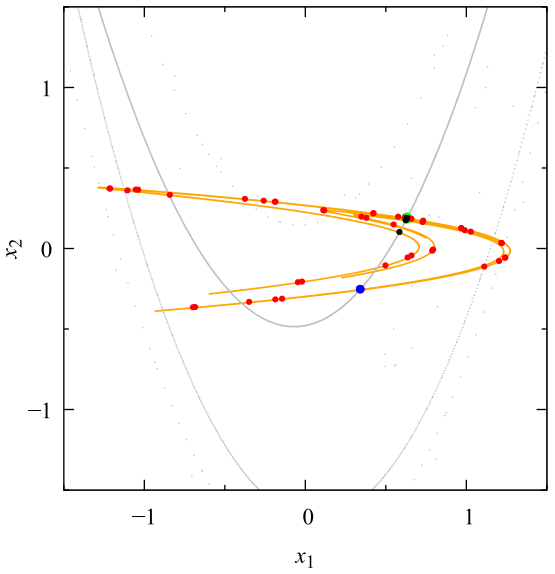

FIGURE 7. Forward images of h_α and backward images of h_ω for I^1 of the Hénon map. The red points indicate the forward images; the black points represent the backward images; the blue points show the homoclinic point at which the forward and backward images arrive; the green point is the 1-periodic point I^1.

by evaluating $\boldsymbol{f}_\lambda^{lM} \circ H_\alpha(z_\alpha)$ for $M \leq 50$ with z_α satisfying the inequality $\|H_\alpha(z_\alpha) - \boldsymbol{x}_p\| = \epsilon$; we select the value of M for which $\|\boldsymbol{f}_\lambda^{lM} \circ H_\alpha(z_\alpha) - \boldsymbol{x}_p\| > 100.0$ is satisfied for the first time. A similar method is followed to select N. It is found here that $M = 50$ is suitable for use for all the unstable manifolds,

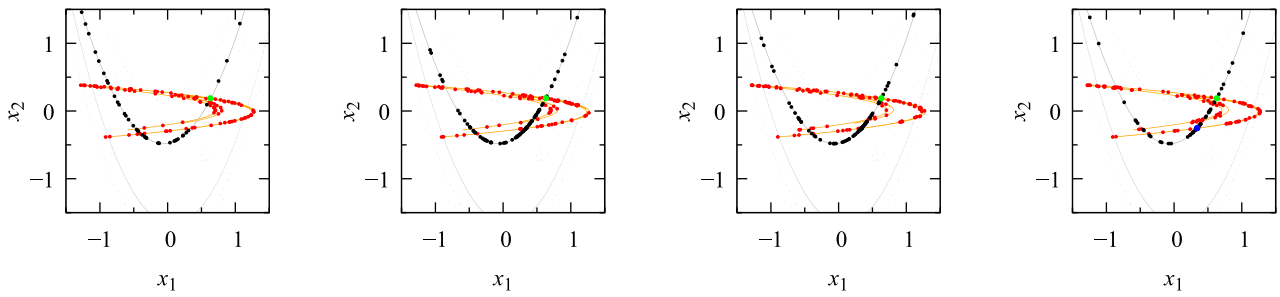

(a) $t = 0$ (start). (b) $t = 200$. (c) $t = 400$. (d) $t = 693$ (end).

FIGURE 8. The convergence of the swarm in the $\mathrm{PSO_{hp}}$ method for I^1 of the Hénon map. Each red point represents the value of $f_\lambda^M \circ H_\alpha\left(z_\alpha^i(t)\right)$ for a single particle; the black points show the values of $f_\lambda^{-N} \circ H_\omega\left(z_\omega^i(t)\right)$ corresponding to each individual particle; the green points show I^1; the blue dot in (d) represents h.

$N = 5$ is suitable for the 1-periodic point, I^1, $N = 3$ is suitable for the 2-periodic point, I^2, and $N = 2$ is suitable for the 4-periodic point, I^4. We note that the algorithm presented here is less sensitive to the selected values of ϵ, the iteration count, or the divergence criterion, provided that the root of the objective function F exists and the value of F does not diverge.

Table 5 shows the results of the numerical experiments undertaken here; the table shows the obtained homoclinic points, $\boldsymbol{h}$, the optimal coefficients γ_α and γ_ω, and the value of the iterator t when the termination criteria are satisfied. The coefficients γ_α and γ_ω can be seen to have norms that are less than $\epsilon(= 0.001)$; we note that $\boldsymbol{h}_\alpha$ and $\boldsymbol{h}_\omega$ satisfy the criterion that they are within the neighborhood of $\boldsymbol{x}_p$.

Table 6 shows the transitions of the images of $\boldsymbol{h}_\alpha$ and $\boldsymbol{h}_\omega$ for I^1. It can be seen that both images of $\boldsymbol{h}_\alpha$ and $\boldsymbol{h}_\omega$ arrive at a single homoclinic point $\boldsymbol{h}$. Fig. 7 shows all the images of $\boldsymbol{h}_\alpha$ and $\boldsymbol{h}_\omega$ in red and black points, respectively. These images transit in $\alpha(I^1)$ and $\omega(I^1)$ and are seen to be coincident at the point shown in blue in Fig. 7; this represents the homoclinic point $\boldsymbol{h}$. We note that all the red and black points shown in Fig. 7 are homoclinic points, despite the fact that they are not observed to be at the intersections of $\alpha(I^1)$ and $\omega(I^1)$ in the figure. To demonstrate that these points are homoclinic points, it would be necessary to calculate further manifolds. Figs. 8 and 9 illustrate the swarm movement that is observed in this implementation of the $\mathrm{PSO_{hp}}$ method; it is seen that the swarm converges to the homoclinic point indicated in Fig. 7. The red and black points in Fig. 8 correspond to the $\mathrm{PSO_{hp}}$ particles in the state space, i.e., $\boldsymbol{f}_\lambda^M \circ H_\alpha(z_\alpha)$ and $\boldsymbol{f}_\lambda^{-N} \circ H_\omega(z_\omega)$, respectively; we note that the points are not z_α and z_ω themselves as they do not represent the points in the state space. Figs. 8(a) to 8(d) show all particles in the state space at $t = 0$, 200, 400, and 693, respectively. As t increases, the swarm gradually approaches the intersections of $\alpha(I^1)$ and $\omega(I^1)$. At $t = 693$, one particle of the swarm converges to a homoclinic point and the termination criterion is met; at this point, the $\mathrm{PSO_{hp}}$ method terminates the calculation. Fig. 9 depicts $H_\alpha(z_\alpha^i(t))$ and $H_\omega(z_\omega^i(t))$ in the neighborhood of I^1.

TABLE 7. Success rates of the proposed method applied to the periodic points in the 2D Hénon map; here, the $\mathrm{PSO_{hp}}$ method was run over 100 trials and the experiment was repeated five times; the mean success rate is also presented.

I^l	1st[%]	2nd[%]	3rd[%]	4th[%]	5th[%]	mean[%]
I^1	30	26	33	26	30	29.0
I^2	37	37	38	36	32	36.0
I^4	21	22	25	15	18	20.2

The blue points in Fig. 9(d) show the positions of $\boldsymbol{h}_\alpha$ and $\boldsymbol{h}_\omega$ that correspond to gbest that is obtained when the search is concluded; the method is seen to terminate with convergence to a single $\boldsymbol{h}_\alpha$ in $\alpha(I^1)$ and a single $\boldsymbol{h}_\omega$ in $\omega(I^1)$. These results indicate that the homoclinic points satisfying (18) can be accurately calculated using the proposed method.

Table 7 shows the success rates calculated in five independent experiments on the same machine for I^1, I^2, and I^4. The reliability of the algorithm presented here was evaluated by considering a metric based on the success rate of the method; this metric was considered in order to take into account the inherent randomness of the $\mathrm{PSO_{hp}}$ method. Here, we classified trials in which the termination criteria were met as successes and other outcomes as failures. These definitions permitted the calculation of the success rate. This resulted in mean success rates of 29.0%, 36.0%, and 20.2% for I^1, I^2, and I^4, respectively. Fig. 10 shows the success rate of the $\mathrm{PSO_{hp}}$ method as a function of the maximum number of iterations, T, from 100 to 100,000; all the rates are calculated considering 500 implementations and random initial values. It can be seen that the success rate of the method proposed here increases as T is increased, reaching approximately 80 % for $T = 100{,}000$. To obtain a satisfactory success rate, we see that it is necessary for T to be set to a large number. We note that the large mapping numbers result in a wide search range. Furthermore, we observe that there exists a countably infinite number of homoclinic points in the state space; all these points can be considered optimal. However, by fixing M, N, and the search space Z^{hp}, the number of homoclinic points

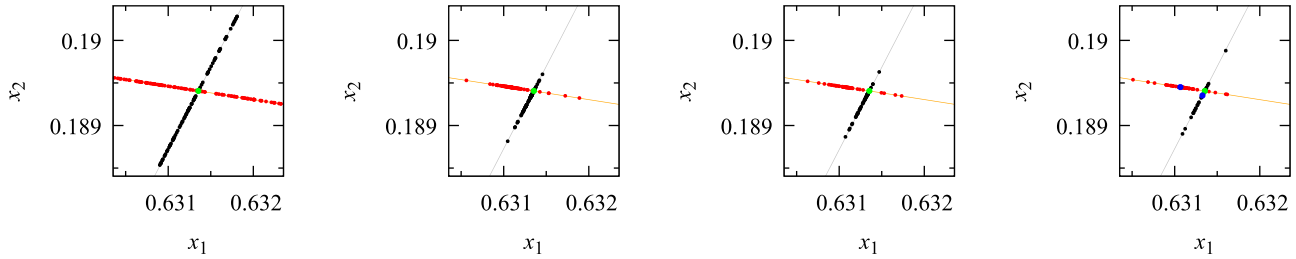

(a) $t = 0$ (start). (b) $t = 200$. (c) $t = 400$. (d) $t = 693$ (end).

FIGURE 9. The convergence of the swarm in the PSO_{hp} method around l^1 (indicated by the green points) of the Hénon map. Each red point represents the value of $H_\alpha(z^i_\alpha(t))$ obtained by an individual particle; the black points show the values of $H_\omega(z^i_\omega(t))$ obtained by a given particle; the blue points in (d) represent the optimal solutions for h_α and h_ω, which correspond to a homoclinic point; the green point represents l^1.

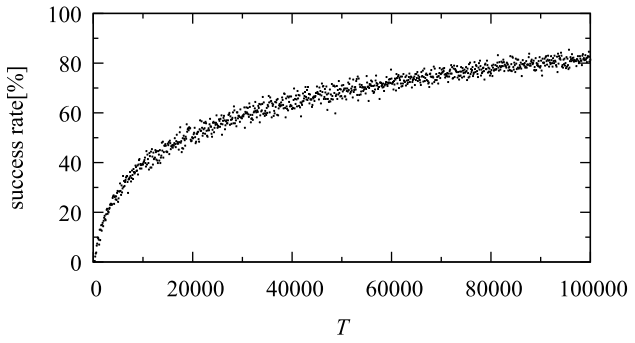

FIGURE 10. Success rate of the PSO_{hp} method per various values of the maximum number of iterations T.

to which the swarm within the PSO_{hp} method can converge becomes finite. This suggests that the number of the optimal homoclinic points that can be obtained by the PSO_{hp} method can be changed by increasing or decreasing the values of M and N, resulting in changes in the convergence speed of the algorithm.

We also investigate whether the PSO_{hp} method can be used to obtain the homoclinic points that are situated near homoclinic tangencies. To this end, we set $\lambda = \langle 1.16, 0.30\rangle$; Fig. 11 shows the resultant unstable and stable manifolds for the 1-periodic saddle point $\boldsymbol{x}_p = \langle 0.67454756, 0.20236426\rangle$. We use the eigenvectors $\boldsymbol{v}_\alpha = \langle 0.985, -0.170\rangle, \boldsymbol{v}_\omega = \langle 0.499, 0.867\rangle$. We can observe that $\alpha(\boldsymbol{x}_p)$ and $\omega(\boldsymbol{x}_p)$ are close to being tangent at their intersections, i.e., the system parameters are close to those that lead to a homoclinic bifurcation. For the homoclinic bifurcation analysis, it is also necessary to obtain the homoclinic points in such a singular case. Table 8 shows the experimental results that can be used in the PSO_{hp} method near the occurrence of a homoclinic tangency. The parameter values that were used to calculate Table 8 are the same as those shown in Table 4; we use the mapping numbers $M = 50$ and $N = 5$. It can be observed from the table that the PSO_{hp} method can be used to calculate the homoclinic points even if the system is in the configuration that is close to a homoclinic tangency. We therefore hypothesize that the PSO_{hp} method can be extended in a manner that will permit the calculations of the homoclinic bifurcation parameters.

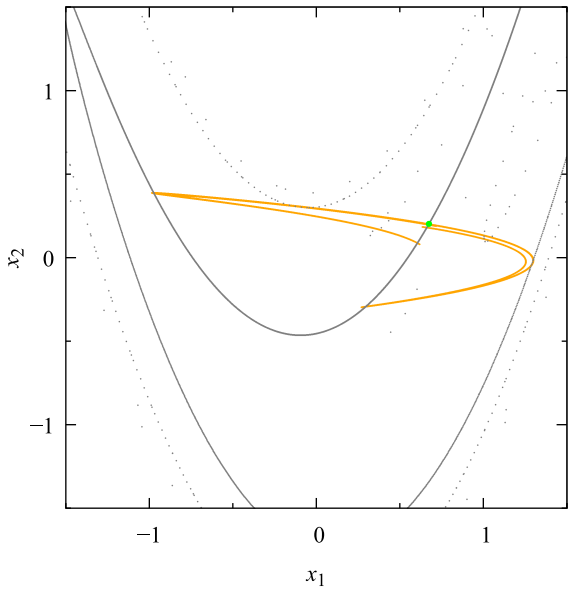

FIGURE 11. Unstable and stable manifolds for a 1-periodic point $\langle 0.67454756, 0.20236426\rangle$ of the Hénon map with $\lambda = \langle 1.16, 0.30\rangle$, having the manifolds near the homoclinic tangency.

TABLE 8. Convergence to the homoclinic point h for the 1-periodic point $x_p = \langle 0.67454756, 0.20236426\rangle$ of the Hénon map with $\lambda = \langle 1.16, 0.30\rangle$ in a configuration close to a homoclinic tangency.

h	γ_α	γ_ω	t
$\langle 0.6064, 0.0892\rangle$	-5.050×10^{-4}	-2.117×10^{-5}	369
$\langle -0.9702, 0.3893\rangle$	-3.542×10^{-4}	-7.099×10^{-4}	589
$\langle 0.2972, -0.2912\rangle$	8.171×10^{-4}	-1.226×10^{-4}	366
$\langle 0.6742, 0.2018\rangle$	-4.620×10^{-4}	-1.099×10^{-7}	243
$\langle 0.2972, -0.2912\rangle$	-3.166×10^{-4}	-1.226×10^{-4}	161

B. CUBIC 3D HÉNON MAP

Here, we utilize the PSO_{hp} method to investigate the properties of the cubic 3D Hénon map [26], which is a 3D discrete-time dynamical system defined by the map $\boldsymbol{f}_\lambda$:

$$\boldsymbol{f}_\lambda : \mathbb{R}^3 \to \mathbb{R}^3,$$
$$\boldsymbol{x} \mapsto \boldsymbol{f}_\lambda(\boldsymbol{x}) = \begin{bmatrix} x_2 \\ x_3 \\ 0.5x_1 + \lambda_1 x_3 + \lambda_2 x_2 - x_2^3 \end{bmatrix} \tag{29}$$

TABLE 9. Convergence to the homoclinic point h for the 1-periodic point $x_p = \langle 0.0, 0.0, 0.0\rangle$ of the cubic 3D Hénon map defined in (29) with $\lambda = \langle -0.75, 1.5\rangle$.

h	γ_α	γ_ω	t
$\langle -1.0316, 0.3389, -0.1043\rangle$	$\langle 3.556\times10^{-4}, -5.988\times10^{-4}\rangle$	8.347×10^{-6}	198
$\langle 1.1991, -1.0316, 0.3389\rangle$	$\langle -2.339\times10^{-4}, -5.567\times10^{-4}\rangle$	-2.731×10^{-5}	277
$\langle -0.3389, 0.1043, -0.0319\rangle$	$\langle 5.406\times10^{-4}, 6.446\times10^{-4}\rangle$	2.551×10^{-6}	171
$\langle -0.0318, 0.0097, -0.0030\rangle$	$\langle -5.789\times10^{-4}, 4.033\times10^{-4}\rangle$	2.379×10^{-7}	192
$\langle -1.2002, 1.0312, -0.3388\rangle$	$\langle -4.751\times10^{-5}, -7.492\times10^{-4}\rangle$	2.730×10^{-5}	796

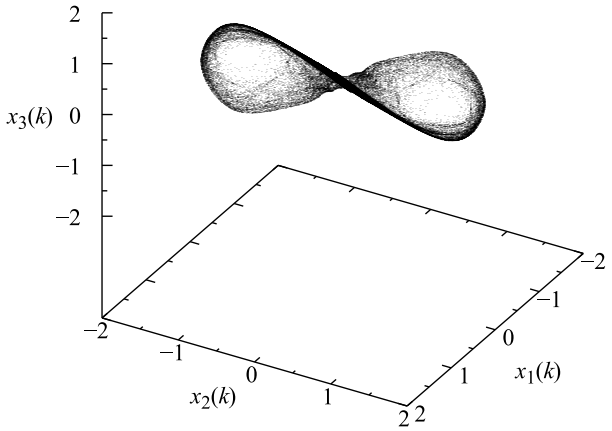

FIGURE 12. Chaotic attractor of the cubic 3D Hénon map defined by (29).

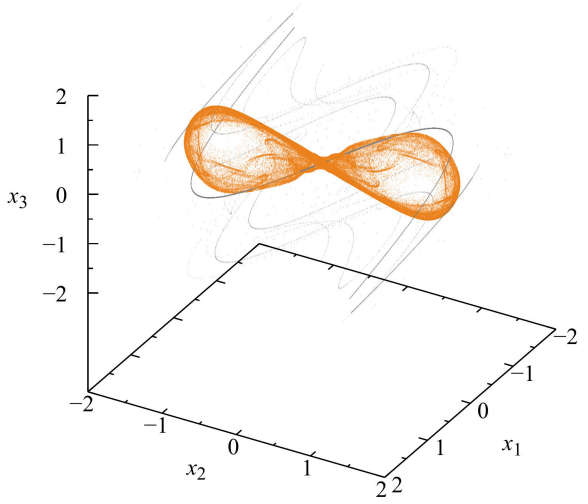

FIGURE 13. 2D unstable manifold (orange) and 1D stable manifold (gray) for $x_p = \langle 0.0, 0.0, 0.0\rangle$ in the cubic 3D Hénon map and $\lambda = \langle -0.75, 1.5\rangle$.

where $\boldsymbol{x} = \langle x_1, x_2, x_3\rangle \in \mathbb{R}^3$ is the state variables vector and $\lambda = \langle \lambda_1, \lambda_2\rangle \in \mathbb{R}^2$ is the system parameters vector. We note that the system investigated here is one of the 3D Hénon maps [27]; the existence of chaotic attractors has been confirmed for $\lambda = \langle -0.75, 1.5\rangle$ [26], as shown in Fig. 12. Here, we calculate the homoclinic points corresponding to a 1-periodic saddle point $\boldsymbol{x}_p = \langle 0.0, 0.0, 0.0\rangle$. The absolute values of two of the eigenvalues associated with $\boldsymbol{x}_p$ are greater than unity, whereas the absolute value of the remaining eigenvalue is less than unity. Therefore, we can conclude that $\boldsymbol{x}_p$ has a 2D unstable manifold and a 1D stable manifold, i.e., $U = 2$ and $S = 1$. We use the eigenvectors

$$\begin{aligned}\boldsymbol{v}_{\alpha 1} &= \langle -0.340, 0.517, -0.786\rangle,\\ \boldsymbol{v}_{\alpha 2} &= \langle -0.535, -0.575, -0.619\rangle,\\ \boldsymbol{v}_{\omega 1} &= \langle -0.953, 0.291, -0.089\rangle.\end{aligned}$$

Fig. 13 shows $\alpha(\boldsymbol{x}_p)$ and $\omega(\boldsymbol{x}_p)$ within the state space; these parameters are indicated by orange and gray points, respectively. Here, the search variable $\boldsymbol{z}_{\rm hp}$ comprises one vector $\boldsymbol{z}_\alpha = \langle z_{\alpha 1}, z_{\alpha 2}\rangle$ and one scalar $z_\omega = z_{\omega 1}$; H_α and H_ω are described by

$$H_\alpha(\boldsymbol{z}_\alpha) = \boldsymbol{x}_p + z_{\alpha 1}\boldsymbol{v}_{\alpha 1} + z_{\alpha 2}\boldsymbol{v}_{\alpha 2}, \tag{30}$$
$$H_\omega(z_\omega) = \boldsymbol{x}_p + z_{\omega 1}\boldsymbol{v}_{\omega 1}. \tag{31}$$

Based on (24), the objective function, F, can be written as

$$F(\boldsymbol{z}_{\rm hp}) = \sqrt{\begin{aligned}&\left[f_1^{lM}\circ H_\alpha(\boldsymbol{z}_\alpha) - f_1^{-lN}\circ H_\omega(z_\omega)\right]^2\\ &+\left[f_2^{lM}\circ H_\alpha(\boldsymbol{z}_\alpha) - f_2^{-lN}\circ H_\omega(z_\omega)\right]^2\\ &+\left[f_3^{lM}\circ H_\alpha(\boldsymbol{z}_\alpha) - f_3^{-lN}\circ H_\omega(z_\omega)\right]^2\end{aligned}}, \tag{32}$$

where $\boldsymbol{f}_\lambda = \langle f_1, f_2, f_3\rangle$. The mapping numbers M and N are selected in the same way as in Section V-A; they are set to be $M = 50$ and $N = 10$. The PSO parameters are set to be equal to those shown in Table 4.

Table 9 shows the results of the numerical experiments undertaken on the cubic 3D Hénon map: the table shows the obtained homoclinic points, $\boldsymbol{h}$, the optimal values of the coefficients $\boldsymbol{g}_\alpha$ and $\boldsymbol{g}_\omega$, and the value of the iterator, t, when the simulation is terminated. We can observe that all the values of the coefficients $\boldsymbol{g}_\alpha$ and $\boldsymbol{g}_\omega$ have a norm of less than unity and $\boldsymbol{h}_\alpha$ and $\boldsymbol{h}_\omega$ are within the neighborhood of $\boldsymbol{x}_p$. Fig. 14 shows the homoclinic point described in the first row of Table 9 together with the unstable and stable manifolds $\alpha(\boldsymbol{x}_p)$ and $\omega(\boldsymbol{x}_p)$. We note that Fig. 14(a) is shown using the same scale as that used in Fig. 13 and the blue point shown in this Fig. 14(a) is the obtained homoclinic

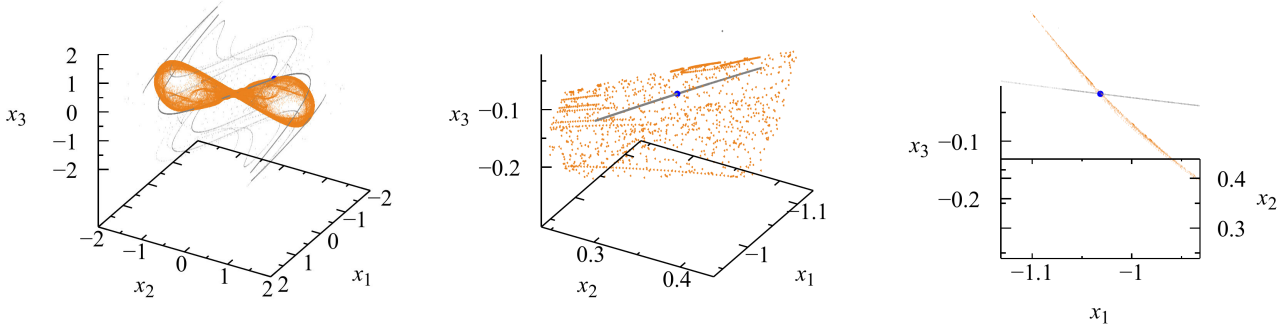

(a) Same scale as Fig. 13 (b) Zoomed-in view near $\boldsymbol{h}$ (c) Different angle of Fig. 14(b)

FIGURE 14. Obtained homoclinic point, h, (indicated by the blue point) for a 1-periodic saddle point $x_P = \langle 0.0, 0.0, 0.0 \rangle$ of the cubic 3D Hénon map with $\lambda = \langle -0.75, 1.5 \rangle$. The orange points represent the points of $x \in \alpha(x_P)$ calculated in this work; the gray points represent the calculated values of $x \in \omega(x_P)$.

TABLE 10. Success rates of the proposed method applied to the periodic points in the 3D Hénon map; here, the PSO_{hp} algorithm was run over 100 trials and repeated over five experiments on separate occasions; the mean success rate is also presented.

1st[%]	2nd[%]	3rd[%]	4th[%]	5th[%]	mean[%]
94	88	90	87	92	90.2

point, $\boldsymbol{h}$. Figs. 14(b) and 14(c) depict the same variables as Fig. 14(a) at a different scale showing the neighborhood of $\boldsymbol{h}$ from two different angles. The orange points can depict a surface defined by the calculated values of $\alpha(\boldsymbol{x}_p)$, and the gray points can be considered as points on the curve of $\omega(\boldsymbol{x}_p)$; the obtained optimal solution can be seen at the intersection of the two features shown in the figure. Therefore, we conclude that the PSO_{hp} method can also be used to obtain the homoclinic points in this 3D discrete-time dynamical system. Table 10 presents the success rates for the method applied to the 3D Hénon map; a mean success rate of 90.2% was found for the proposed method, which represents a significant improvement on the rates presented in Section V-A for the 2D case. We hypothesize that the difference in the performance of the algorithm when used to study these two systems is due to the system characteristics; in particular, the number of the optimal homoclinic points of the objective functions differs between the dynamical systems. This implies that the values of M and N must be selected carefully for each individual system. We note that the same values of these parameters were used in the implementations presented in this work as these values were found to be appropriate for both systems. Based on the work presented here, no correlations can be observed between the dimension of the system state space and the success rate of the proposed method. On the other hand, we note that an increase in the dimensionality of the search may mean that the number of iterations until convergence increases. It is confirmed here that the proposed method is suitable to find homoclinic points in this 3D discrete-time dynamical system without significant alterations to the algorithm. This suggests that it is plausible that the method can be applied to systems of higher dimensionality.

VI. CONCLUSION

In this work, an algorithm to obtain homoclinic points was proposed based on the PSO method. An n-dimensional discrete dynamical system, as well as its unstable and stable manifolds and homoclinic points, was defined. We proposed an algorithm that can be used to obtain homoclinic points, named the PSO_{hp} method, including a new search space and an objective function; these elements were defined such that they satisfy the criteria for homoclinic points to exist. We applied the proposed method to two discrete-time dynamical systems: the Hénon map and the cubic 3D Hénon map. Via the implementation of this method on these systems, we confirmed the effectiveness of this method. It was demonstrated that the PSO_{hp} method can be used to obtain the homoclinic points for parameters that describe the system that are close to those that lead to a homoclinic tangency within the system. Unlike conventional PSO methods that often suffer from slow convergence near homoclinic bifurcation parameters, the proposed method exhibited no such difficulties. The methodology utilizes the capacity of the PSO method to generate random initial values, which facilitates the computation of homoclinic points without any prerequisites being placed on the selection of the initial conditions used. While the proposed method involves an increased number of iterations and objective function computations, it removes the requirement for selecting appropriate initial values, thereby offering a significant advantage in applications where such selection is non-trivial or dependent on specific expertise. The proposed method is expected to be applicable to discrete dynamical systems of any dimension and of any period without significant modifications to the algorithm or the objective function. The method was found to work well without carefully chosen initial conditions or information regarding the derivatives of the objective functions, e.g. Hessian tensor. Eliminating the necessity of carefully selecting the initial values used and obtaining information regarding the derivatives of the objective function is advantageous in numerous practical scenarios, such practical situations include those that involve

computationally intensive simulations and/or when dealing with discontinuous dynamical systems. In particular, the proposed method is expected to be suitable for obtaining the homoclinic points for high-dimensional dynamical systems as it does not require any careful choice of initial values; the previously developed algorithms have been largely unsuitable for application on such systems. Therefore, we conclude that the proposed method facilitates the analysis of dynamical systems, reducing issues associated with the sensitivity of alternative methods to initial values and the calculation of the derivatives of the objective function; we thus believe that the method presented here will serve as a fundamental tool within future research. The success rates would depend on the features of the optimization algorithms. However, the main purpose of this study is to propose a detection method for homoclinic points using metaheuristic derivative-free optimization. Since most researchers, who are experts in bifurcation analysis, are not experts in swarm intelligence, the authors think that simpler derivative-free optimizations such as PSO are better for bifurcation analysis in terms of usability. In fact, our PSO-based algorithm has been successful in deriving homoclinic points with high accuracy. On the other hand, a higher success rate could be achieved by applying other derivative-free algorithms with higher search capability than PSO to the proposed method. In future works, there are four primary issues to solve. First, future development efforts will have the aim of extending the method presented here to problems related to the determination of homoclinic bifurcation parameters within discrete-time dynamical systems. The goal of such a future study would be to create an algorithm that is capable of deriving the homoclinic bifurcation sets of a system; we note that the ideal method would not require the careful selection of initial values or information regarding the derivatives of the objective functions. The second extension of this work would be related to the homoclinic points observed in continuous-time dynamical systems. A third area that should be investigated in future is related to the underlying causes of the significant difference in the success rate of the method when it is applied to 2D and 3D systems. Fourthly, we compare the standard PSO used in this study with other optimizers. Future work related to these four points will undoubtedly improve the PSO_{hp} method by making it more general and compatible with a wider range of nonlinear dynamical systems.

REFERENCES

[1] E. N. Lorenz, "Deterministic nonperiodic flow," *J. Atmos. Sci.*, vol. 20, no. 2, pp. 130–141, Mar. 1963, doi: 10.1175/1520-0469(1963)020<0130:DNF>2.0.CO;2.

[2] E. M. Izhikevich, "Simple model of spiking neurons," *IEEE Trans. Neural Netw.*, vol. 14, no. 6, pp. 1569–1572, Nov. 2003, doi: 10.1109/TNN.2003.820440.

[3] T. Matsumoto, "A chaotic attractor from Chua's circuit," *IEEE Trans. Circuits Syst.*, vol. CS-31, no. 12, pp. 1055–1058, Dec. 1984, doi: 10.1109/TCS.1984.1085459.

[4] F. Pellestor, J. Gaillard, A. Schneider, J. Puechberty, and V. Gatinois, "Chromoanagenesis, the mechanisms of a genomic chaos," *Seminars Cell Develop. Biol.*, vol. 123, pp. 90–99, Mar. 2022, doi: 10.1016/j.semcdb.2021.01.004.

[5] H. Liu and S. Vardhan, "A dynamical mechanism for the page curve from quantum chaos," *J. High Energy Phys.*, vol. 2021, no. 3, pp. 1–35, Mar. 2021, doi: 10.1007/jhep03(2021)088.

[6] J. S. Teh, M. Alawida, and Y. C. Sii, "Implementation and practical problems of chaos-based cryptography revisited," *J. Inf. Secur. Appl.*, vol. 50, Feb. 2020, Art. no. 102421, doi: 10.1016/j.jisa.2019.102421.

[7] Z. Ahmad, F. Ali, N. Khan, and I. Khan, "Dynamics of fractal-fractional model of a new chaotic system of integrated circuit with Mittag–Leffler kernel," *Chaos, Solitons Fractals*, vol. 153, Dec. 2021, Art. no. 111602, doi: 10.1016/j.chaos.2021.111602.

[8] N. Khan, Z. Ahmad, H. Ahmad, F. Tchier, X.-Z. Zhang, and S. Murtaza, "Dynamics of chaotic system based on image encryption through fractal-fractional operator of non-local kernel," *AIP Adv.*, vol. 12, no. 5, May 2022, Art. no. 055129, doi: 10.1063/5.0085960.

[9] Y. Niu and L. Sheng, "Uniform quantized synchronization for chaotic neural networks with successive packet dropouts," *Asian J. Control*, vol. 21, no. 1, pp. 639–646, Jan. 2019, doi: 10.1002/asjc.1736.

[10] S. Smale, "Differentiable dynamical systems," *Bull. Amer. Math. Soc.*, vol. 73, no. 6, pp. 747–817, 1967.

[11] H. Kawakami and J. Matsuo, "Computation of doubly asymptotic motions," in Japanese, *Trans. Inst. Electron. Commun. Eng. Jpn.*, vol. 64, no. 12, pp. 1058–1059, Dec. 1981.

[12] H. Kawakami and J. Matsuo, "Bifurcation of doubly asymptotic motions in nonlinear systems," in Japanese, *The Trans. Inst. Electron. Commun. Eng. Jpn.*, vol. 65, no. 7, pp. 647–654, Jul. 1982.

[13] A. R. Champneys, Y. A. Kuznetsov, and B. Sandstede, "A numerical toolbox for homoclinic bifurcation analysis," *Int. J. Bifurcation Chaos*, vol. 6, no. 5, pp. 867–887, May 1996, doi: 10.1142/s0218127496000485.

[14] A. R. Champneys and Y. A. Kuznetsov, "Numerical detection and continuation of codimension-two homoclinic bifurcations," *Int. J. Bifurcation Chaos*, vol. 4, no. 4, pp. 785–822, Aug. 1994, doi: 10.1142/s0218127494000587.

[15] N. Neirynck, W. Govaerts, Y. A. Kuznetsov, and H. G. E. Meijer, "Numerical bifurcation analysis of homoclinic orbits embedded in one-dimensional manifolds of maps," *ACM Trans. Math. Softw.*, vol. 44, no. 3, pp. 1–19, Jan. 2018, doi: 10.1145/3134443.

[16] H. Matsushita, Y. Tomimura, H. Kurokawa, and T. Kousaka, "Period doubling bifurcation point detection strategy with nested layer particle swarm optimization," *Int. J. Bifurcation Chaos*, vol. 27, no. 7, Jun. 2017, Art. no. 1750101, doi: 10.1142/s0218127417501012.

[17] H. Matsushita, H. Kurokawa, and T. Kousaka, "Bifurcation analysis by particle swarm optimization," *Nonlinear Theory Appl. IEICE*, vol. 11, no. 4, pp. 391–408, Oct. 2020, doi: 10.1587/nolta.11.391.

[18] J. Kennedy and R. Eberhart, "Particle swarm optimization," in *Proc. Int. Conf. Neural Netw.*, Perth, WA, Australia, Nov. 1995, pp. 1942–1948, doi: 10.1109/ICNN.1995.488968.

[19] T. Gotoh, H. Kurokawa, H. Matsushita, and T. Kousaka, "Neimark-sacker bifurcation points derivation method in nonlinear dynamical systems using nested-layer particle swarm optimizations," *IEEJ Trans. Electron., Inf. Syst.*, vol. 142, no. 6, pp. 670–678, Jun. 2022, doi: 10.1541/ieejeiss.142.670.

[20] H. Matsushita, W. Kinoshita, H. Kurokawa, and T. Kousaka, "Particle swarm optimization-based strategy for detecting border-collision bifurcation points in piecewise smooth maps," *Appl. Soft Comput.*, vol. 95, Oct. 2020, Art. no. 106319, doi: 10.1016/j.asoc.2020.106319.

[21] T. Makino, Y. Miino, H. Matsushita, and T. Kousaka, "Computation of homoclinic points using particle swarm optimization in 2-dimensional discrete dynamical systems," in *Proc. 19th Int. SoC Design Conf. (ISOCC)*, Oct. 2022, pp. 267–268, doi: 10.1109/ISOCC56007.2022.10031372.

[22] T. Makino, Y. Miino, H. Matsushita, and T. Kousaka, "A calculation of homoclinic points for periodic points with PSO," in *Proc. Int. Symp. Nonlinear Theory Appl.*, 2023, p. 535, doi: 10.34385/proc.76.C3L-22.

[23] B. Liu, L. Wang, Y.-H. Jin, F. Tang, and D.-X. Huang, "Directing orbits of chaotic systems by particle swarm optimization," *Chaos, Solitons Fractals*, vol. 29, no. 2, pp. 454–461, Jul. 2006, doi: 10.1016/j.chaos.2005.08.034.

[24] M. Hénon, "A two-dimensional mapping with a strange attractor," *Commun. Math. Phys.*, vol. 50, no. 1, pp. 69–77, Feb. 1976, doi: 10.1007/bf01608556.

[25] I. C. Trelea, "The particle swarm optimization algorithm: Convergence analysis and parameter selection," *Inf. Process. Lett.*, vol. 85, no. 6, pp. 317–325, Mar. 2003, doi: 10.1016/s0020-0190(02)00447-7.

[26] A. S. Gonchenko and S. V. Gonchenko, "Variety of strange pseudo-hyperbolic attractors in three-dimensional generalized Hénon maps," *Phys. D, Nonlinear Phenomena*, vol. 337, pp. 43–57, Dec. 2016, doi: 10.1016/j.physd.2016.07.006.
[27] S. V. Gonchenko, I. I. Ovsyannikov, C. Simó, and D. Turaev, "Three-dimensional Hénon-like maps and wild Lorenz-like attractors," *Int. J. Bifurcation Chaos*, vol. 15, no. 11, pp. 3493–3508, Nov. 2005, doi: 10.1142/s0218127405014180.

TATSUMI MAKINO received the B.E. degree from the Department of Electrical and Electronic Engineering, Chukyo University, Aichi, Japan, in 2022. His research interest includes the establishment of the bifurcation analysis method with an optimization technique.

YUU MIINO (Member, IEEE) received the B.E., M.E., and Ph.D. degrees in nonlinear engineering from Tokushima University, Japan, in 2014, 2016, and 2019, respectively.

From 2019 to 2022, he was an Assistant Professor with Tokyo University of Technology. Since 2022, he has been a Lecturer with Naruto University of Education. He is the author of one book and more than 70 academic articles. His research interests include hybrid dynamical systems, local and global bifurcation problems, chaos, fractals, and symbolic dynamical systems. He is an Associate Editor of the *NOLTA* (IEICE), Special Section on Recent Progress in Nonlinear Theory and Its Applications. He was a recipient of the 2022 IEEE CASS Shikoku Chapter Young Researcher Award and the Best Student Paper Award of the 2017 International Symposium on Nonlinear Theory and Its Applications.

HARUNA MATSUSHITA (Member, IEEE) received the B.E., M.E., and Dr.Eng. degrees in electrical and electronic engineering from Tokushima University, Japan, in 2005, 2007, and 2008, respectively. In 2011, she joined the Department of Electronics and Information Engineering, Kagawa University, Kagawa, Japan, where she has been an Associate Professor, since April 2020. Her research interests include nonlinear optimization by swarm intelligence and its application. She is a member of the IEICE and RISP.

TAKUJI KOUSAKA (Member, IEEE) received the Ph.D. degree from Tokushima University, in 1999. In 1999, he joined Fukuyama University, Japan. He was an Associate Professor with the Department of Mechanical and Energy Systems Engineering, Oita University, from 2006 to 2017. He is currently a Professor in the electrical and electronic engineering with Chukyo University, Japan. His research interests include bifurcation analysis in the switched dynamical systems and its application.